Nanoscale Horizons

ROYAL SOCIETY OF CHEMISTRY

COMMUNICATION

View Article Online
View Journal | View Issue

Cite this: *Nanoscale Horiz.*, 2025, **10**, 2931

Received 13th May 2025,
Accepted 1st July 2025

DOI: 10.1039/d5nh00338e

rsc.li/nanoscale-horizons

Adjustable SiC interfacial layers toward reliable Si-based anode applications†

Wenhui Lai,‡[a] Jong Hak Lee,‡[b] Yue Yuan,[c] Yong Kang Ong,[b] Carlos Limpo,[a] Lu Shi,[a] Yanhui Pu,[a] Yifan Rao,[a] Mario Lanza[abe] and Barbaros Özyilmaz *[abde]

The incorporation of a SiC interfacial layer has been recognized as an effective strategy to tackle the interface contact issue between Si and carbon, ensuring the structural integrity of Si-based anodes and thereby enhancing their cycling stability. However, its inherent low activity and poor conductivity pose a persistent challenge for maximizing capacity and facilitating ion and electron transport. Here, we present a thickness/content adjustable SiC interfacial layer in the Si–SiC–C heterostructure using a modified spark plasma sintering technique. The SiC layer, with a content of ~10%, is discretely coated on the surface of the Si core, exerting minimal influence on capacity and ion/electron kinetics, while ensuring high electrode structural stability. Consequently, the Si-based anode exhibits a stable capacity of 582 mAh g^{-1} (0.1 A g^{-1}) and good rate capability (324 mAh g^{-1} at 2 A g^{-1}), while maintaining 80% capacity retention over 500 cycles with a low electrode swelling of 12.6%. More importantly, its capacity presents a continuous rising trend with the increase of the cycle number, suggesting a mechanism where the SiC interfacial layer gradually transforms into a Li-ion-rich phase. This transformation facilitates ion transport and reaction with Si, resulting in gradual capacity enhancement. Therefore, the reasonably thickness-regulated SiC interfacial layer holds promise for providing inspiration for the design of commercial Si-based anodes.

New concepts

This work introduces a new interfacial engineering concept by transforming insert SiC into a multifunctional phase that actively governs lithium-ion transport, interfacial stability, and structural integrity within Si-based anodes. Unlike conventional strategies that use SiC as a passive coating, we demonstrate that an in situ-formed nanoscale SiC layer—generated through a scalable spark plasma sintering (SPS) process—acts as a lithium-ion modulator and mechanical buffer. More importantly, the Si/SiC heterointerface enhances ionic accessibility and mitigates continuous SEI growth, contributing to long-term performance and high electrode stability. This dual-functionality of SiC represents a conceptual shift in how interphases are designed in alloy-type anodes, enabling synergistic tuning of both chemical and mechanical failure pathways. The approach provides new insights into nanostructured interfacial design and highlights a previously underexplored role of stable ceramic phases in regulating dynamic ion transport. It further offers a promising route toward scalable, high-energy-density batteries for practical applications. This concept may inspire broader adoption of multifunctional interphases in nanoscience, where traditionally "insert" materials can be re-envisioned as active components in next-generation energy technologies.

Introduction

Despite experiencing substantial volumetric changes (up to 400%) during lithiation and delithiation, silicon (Si) remains one of the most promising anode materials for lithium-ion batteries (LIBs) due to its theoretical capacity, which is approximately ten times greater than that of commercial graphite (4200 mAh g^{-1} *vs.* 372 mAh g^{-1}).[1,2] This exceptional capacity makes it a highly attractive candidate, particularly for applications in high-performance electric vehicles (EVs), where LIBs with high energy density are critical to meeting the increasing demands for longer driving ranges. Currently, industrial Si-based anodes typically employ a straightforward blending technology that combines a low proportion of silicon oxide (SiO_x, 2–10 wt%) with graphite (known for its high cycling stability, excellent conductivity, and low expansion rate) to solve its intrinsic expansion challenge.[3] While this approach ensures some level of stability, the relatively low Si content limits the overall capacity of Si-based anodes, resulting in an energy density of <300 Wh kg^{-1} for the battery

[a] *Department of Material Science and Engineering, National University of Singapore, Singapore 117575, Singapore. E-mail: barbaros@nus.edu.sg*
[b] *Center for Advanced 2D Materials, National University of Singapore, Singapore 117546, Singapore*
[c] *Materials Science and Engineering Program, Physical Science and Engineering Division, King Abdullah University of Science and Technology (KAUST), Thuwal 23955-6900, Saudi Arabia*
[d] *Department of Physics, National University of Singapore, Singapore 117551, Singapore*
[e] *Institute for Functional Intelligent Materials, National University of Singapore, Singapore 117544, Singapore*

† Electronic supplementary information (ESI) available. See DOI: https://doi.org/10.1039/d5nh00338e

‡ These authors contributed equally: Wenhui Lai, Jong Hak Lee.

and an endurance mileage of <500 km for the current EVs.[4] To enhance the energy density and extend the range, increasing the Si content is essential, but this requires a redesign of the interface between Si and carbon materials.[5–9] The challenge lies in the fact that as the Si content increases, the volume expansion during cycling becomes more pronounced, amplifying the mechanical stress on the electrode. Without an effective and robust electrical contact at the Si–carbon interface, the electrode's integrity is compromised, particularly after the pulverization of Si particles. This degradation leads to a rapid loss of capacity and eventually results in battery failure. Therefore, addressing the interface stability between Si and carbon is crucial to enabling high-Si-content anodes for the next generation of high-performance LIBs.

Recently, silicon carbide (SiC) has been proposed as an interfacial layer to effectively address the interface contact challenge between Si and carbon, thereby preserving the structural integrity and long-term stability of the Si-based anodes.[10–13] Notably, SiC exhibits exceptional mechanical (hardness: 35–45 GPa), thermal (coefficient of thermal expansion: 4×10^{-6} °C^{-1}), and chemical stabilities.[14] The remarkable mechanical properties of SiC confer high strength and toughness, enabling it to function as a resilient matrix, structural reinforcement layer, or buffer layer within the Si-based anodes.[15,16] This allows it to withstand the internal stresses caused by the volume expansion and shrinkage of Si, thereby mitigating the pulverization of particles. More importantly, SiC consistently retains a strong adhesion between Si and carbon during the lithiation and delithiation processes, suppressing void evolution and maintaining persistent electrical contact even in instances of Si breakage.[10–12] Additionally, the thermal expansion coefficient of SiC is closely matched to that of Si (3×10^{-6} °C^{-1}).[14] When SiC serves as the interface protective layer for Si, it assists in decreasing residual stress and preventing spontaneous cracking, resulting in enhanced thermal stability for Si-based anodes. Moreover, the SiC interfacial layer exhibits high chemical stability toward the electrolyte.[17–19] This chemical inertness contributes to the passivation of the Si surface, reducing its direct exposure to electrolyte salts. Consequently, it significantly suppresses side reactions between Si and the electrolyte, such as the formation of Li_2SiF_6, by raising the activation energy of these detrimental processes. This suppression reduces the degradation of the Si anode, leading to improved cycling stability and enhanced electrochemical performance over extended use.[19]

However, the presence of SiC in Si-based anodes tends to decrease the specific capacity and lower the transport efficiency of Li ions/electrons, which is often overlooked, especially in the case of the heterogeneous structure of Si–SiC–C. As a traditional wide band gap semiconductor, SiC adopts a layered stacked crystal structure with strong covalent bonds.[20,21] Consequently, it exhibits intrinsic low electronic conductivity and high surface lithiation energy, resulting in limited charge transfer kinetics and negligible lithiation ability. Although it has been demonstrated that Li ions can occupy the interstitial or vacancy sites of the SiC lattice, thus providing it with a certain Li-ion storage capability, the extremely scarce number of sites and narrow transport channels greatly hinder the storage capacity and decelerate the lithiation kinetics.[22,23] Unfortunately, this also poses challenges for Li ions to migrate from these sites during the delithiation process, leading to the formation of dead Li.[23] Moreover, the excessive formation of SiC inevitably consumes a substantial amount of Si, and the presence of a SiC intermediate layer significantly impedes the contact and reaction between Li ions and the inner Si cores.[11] As a result, these factors collectively contribute to a decrease in the overall capacity of Si-based anodes.

Hence, by reasonably adjusting the thickness or content of the SiC interfacial layer in Si-based anodes, optimal structural stability can be achieved while minimizing the impact on capacity and ion/electron transport kinetics. This strategy is anticipated to further enhance the proportion of Si in industrial Si-based anodes. In this work, we employ modified spark plasma sintering (SPS) technology to process reduced graphene oxide and Si composite (RGO/Si) with Joule heat generated by pulsed current as a radiation source. By regulating the SPS temperature to 500, 650, and 800 °C, three kinds of Si-based composites (Si content: $\sim$20 wt%) are prepared, denoted as S500, S650, and S800, respectively. After confirming the presence and content of SiC in Si-based composites, we investigate their corresponding physicochemical properties, electrochemical performance, and electrode swelling. As a result, with the increase of SPS temperature, the SiC content in Si-based composites also rises, leading to improved structural stability in Si-based anodes. However, this increment correlates with a declining trend in their specific capacity. Therefore, the S800 anode exhibits the lowest capacity of 325 mAh g^{-1} (0.1 A g^{-1}) and the highest cycle life (800 cycles, with 80% capacity retention at 2 A g^{-1}), while the S500 anode delivers the highest capacity of 674 mAh g^{-1} and the lowest cycle life (150 cycles). In contrast, the S650 anode with a SiC content of 10.2% is capable of both a stable output capacity (582 mAh g^{-1}) and excellent cycling stability (500 cycles). These findings suggest that, by introducing $\sim$10% SiC content into the Si–SiC–C heterostructure, the interfacial stability of Si-based anodes is effectively enhanced while maintaining sufficient capacity and favorable kinetics.

Results

Fabrication of Si-based composites with different SiC content

To construct the heterogeneous layered structure of Si–SiC–C, we selected RGO and amorphous micron-sized Si as our starting materials, both of which possess numerous intrinsic defects.[24,25] Following the preparation of homogeneous RGO/Si composites through high-energy ball milling (HEBM), modified SPS technology was employed to regulate the thickness/content of the SiC interfacial layer. As shown in Fig. 1(a), the modified SPS system utilizes pulsed current as a radiation source to generate Joule heat on the powder, while simultaneously exerting pressure directly to achieve rapid and uniform sintering.[26] By controlling different SPS temperatures, four types of Si-based composites, including RGO/Si (untreated), S500 (SPS temperature: 500 °C), S650 (SPS temperature: 650 °C), and S800 (SPS temperature: 800 °C), were readily prepared.

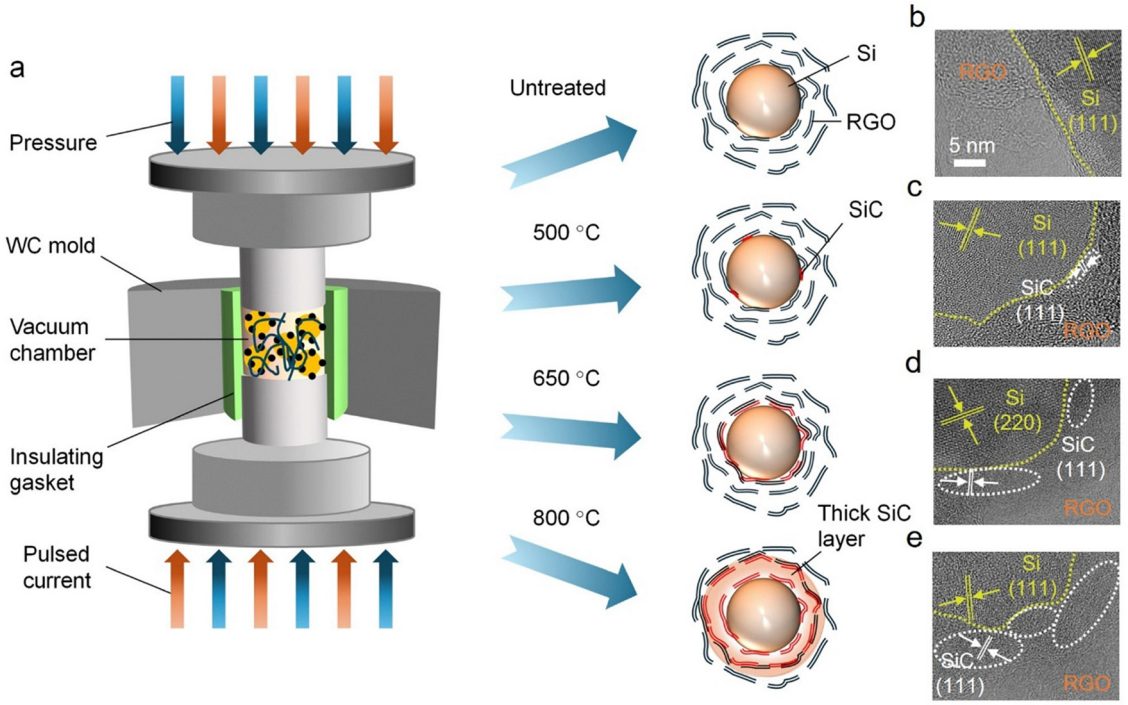

Fig. 1 Schematic diagram of the preparation of Si-based composites by modified SPS technology. (a) Diagrammatic illustration of the modified SPS system and different RGO/Si composites prepared by adjusting the SPS temperature. (b)–(e) High-resolution TEM images of RGO/Si, S500, S650, and S800. Scale bars, 5 nm (b)–(e).

Through high-resolution transmission electron microscope (TEM) observation (Fig. 1(b)–(e)), we found that the SiC thickness was different in these four Si-based composites. The lattice distances of 0.31 nm and 0.34 nm were observed in the RGO/Si sample (Fig. 1(b)), corresponding to the (111) and (002) planes of Si and RGO, respectively. In the S500, S650, and S800 samples, there was a new lattice distance ordering of 0.25 nm between Si and RGO, corresponding to the (111) crystal face of SiC (Fig. 1(c)–(e)). In addition, the electron energy loss spectroscopy (EELS) of the Si L-edge revealed a significant shift of the Si peak at 100.5 eV towards higher electron energy loss in the S500 sample, compared to the RGO/Si sample (ESI,† Fig. S1). Moreover, peaks at 105.7 eV, which are characteristic of SiC, were detected in the S650 and S800 samples. These spectral shifts and peaks strongly support the formation of SiC in the SPS-treated samples. More importantly, the thickness of the SiC layer in these samples exhibited an increasing trend with the rise in SPS temperature. In the S500 and S650 samples, the SiC layers were dispersed discretely on the surface of Si, with the thickness increasing from 1–3 nm to 3–5 nm. However, in the S800 sample, most of the surface of the Si was covered by the SiC layer, exhibiting a thickness of 5–10 nm.

Notably, conventional methods for producing SiC typically involve high temperatures (>1400 °C) or necessitate the use of expensive chemical vapor deposition (CVD) processes and specific catalysts/nucleating agents.[10,11,27] In contrast, our method does not require such harsh synthesis conditions and enables SiC formation at low temperatures. The reasons for this phenomenon are believed to be as follows: (a) the modified SPS technology allows the current to directly pass through the powder, resulting in an interfacial temperature that is much higher than the set temperature (*e.g.*, 500 °C) due to the high interfacial resistance between the particles.[28] (b) The existence of a large number of defects in RGO and amorphous Si potentially promotes the nucleation and growth of SiC.[11,29] (c) The nanoscale effect arising from the utilization of nanometer-sized raw materials further facilitates SiC formation.[30] (d) Due to the presence of numerous pores resulting from the combination of Si particles with RGO, the actual local pressure at the Si–RGO interface under the SPS pressure exceeds the set value (*e.g.*, 120 MPa).[31] Therefore, this process of SiC generation appears to be simple and feasible, making it suitable for large-scale industrial production.

Verification of SiC content in Si-based composites

As shown in Fig. 2, X-ray diffractometer (XRD), X-ray photoelectron spectroscopy (XPS), and thermal gravimetric analysis (TGA) were conducted to confirm the specific SiC content in Si-based composites (RGO/Si, S500, S650, and S800). XRD patterns validated that the phases of Si and carbon in the Si-based composites corresponded to PDF no. 27-1402 and PDF no. 26-1076, respectively (Fig. 2(a)). Additionally, the presence of SiC phase was successfully detected in S650 and S800 samples. From the amplified XRD pattern, it was observed that the peak area corresponding to the SiC (111) crystal face gradually increased from S500 to S650 and then to S800, indicating a gradual increase in SiC content (Fig. 2(b)). Subsequently, the content of Si–C bond in Si-based composites was assessed based on XPS spectra (Fig. 2(c) and (d)). As shown in the

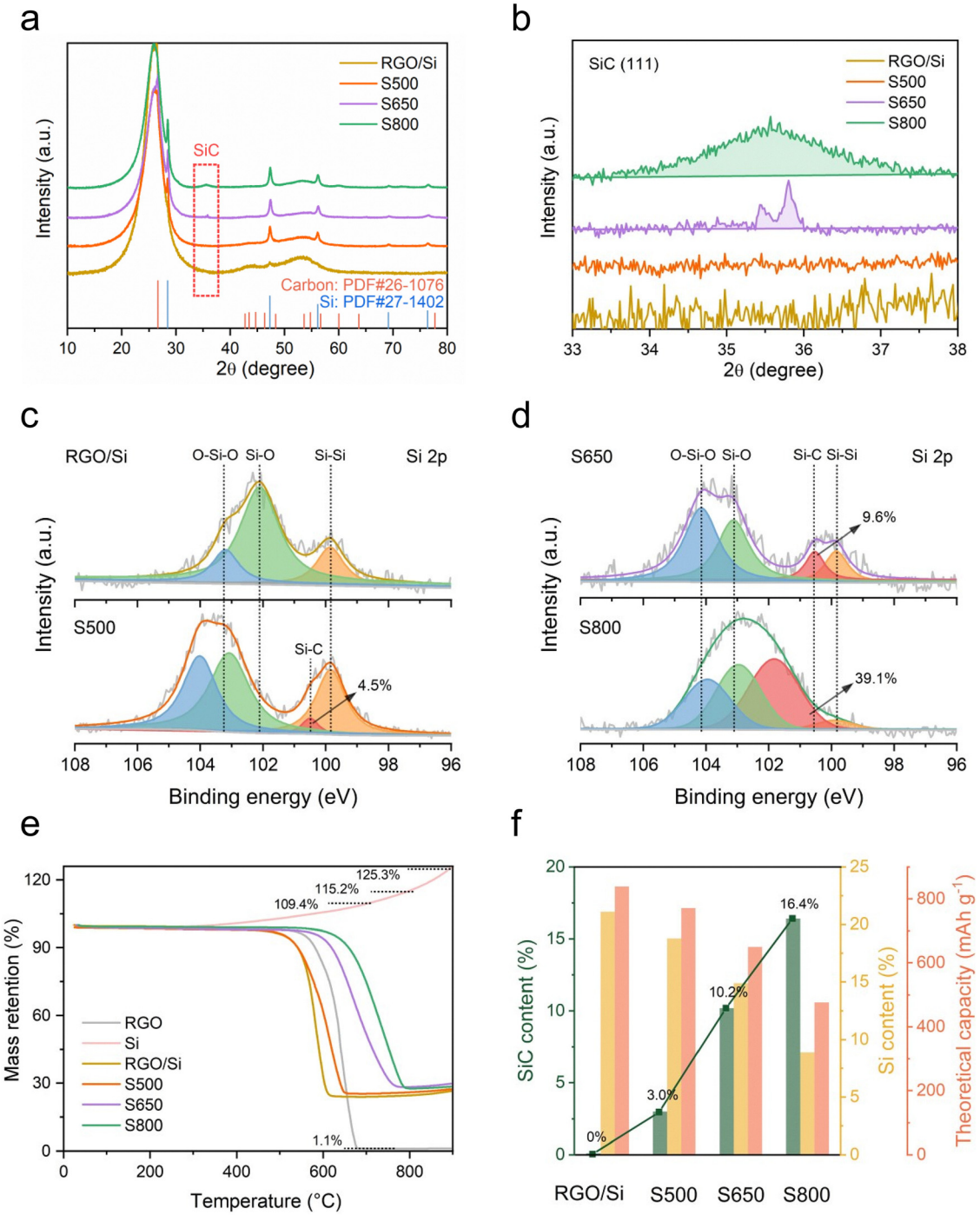

Fig. 2 Determination of SiC content in Si-based composites. (a) XRD patterns of RGO/Si, S500, S650, and S800 samples. (b) Amplified XRD patterns in the SiC (111) region. (c) and (d) Si 2p XPS spectra comparison of RGO/Si, S500, S650, and S800. (e) TGA curves of RGO, Si, RGO/Si, S500, S650, and S800. (f) SiC content, Si content, and theoretical capacity comparison in the Si-based composites.

Si 2p region, a new characteristic peak appeared at 100.5 eV (shift to 101.8 eV for S800) after the modified SPS treatment, corresponding to the Si–C bond. Moreover, with the increase of SPS temperature, the proportion of Si–C bond in all Si 2p orbital peaks increased, reaching 4.5%, 9.6%, and 39.1% for S500, S650, and S800 samples, respectively. As a consequence, we have confirmed from high-resolution TEM, EELS, XRD, and XPS characterization that SiC was indeed generated in S500, S650, and S800 samples, and the SiC content demonstrated an increasing trend with the rise of SPS temperature.

In order to quantitatively analyze the SiC content, we performed TGA characterization of Si-based composites (Fig. 2(e) and (f)) with the specific analysis method in Note S1 and Tables S1, S2 (ESI†). Given the limited presence of native SiO_x and the

fact that SPS is conducted under vacuum, no additional Si–O bonds are formed, nor are existing ones disrupted (the experimental temperature lower than the threshold required for carbothermal reduction of SiO_x).[32] As the bond energy of Si–O is significantly higher than that of Si–Si, it is reasonable to assume that Si–Si bonds are preferentially consumed during SiC formation.[33] Accordingly, in the TGA analysis, SiO_x is not treated as a separate component; any minor contribution from SiO_x (typically accounting for less than 3 wt%) is considered part of the estimated SiC content,[34] which does not affect the interpretation of the relative trend in SiC evolution. Based on the TGA curves of RGO, Si, RGO/Si, S500, S650, and S800 depicted in Fig. 2(e), the mass retention of each sample at specific temperatures (*e.g.*, 700, 800, and 895 °C) was determined, as illustrated in Table S1 (ESI†). By constructing mathematical equations (see details in Note S1, ESI†), we could then calculate the specific content of C, Si, and SiC in RGO/Si, S500, S650, and S800 samples, as shown in Fig. 2(f) and Table S2 (ESI†). The proportion of SiC content in RGO/Si, S500, S650, and S800 samples was 0%, 3.0%, 10.2%, and 16.4%, respectively, showing an increasing trend, which was consistent with the results of TEM, XRD, and XPS. Correspondingly, the Si content decreased in Si-based composites due to the consumption of Si for SiC formation, leading to a corresponding decrease in their theoretical specific capacity. Specifically, the theoretical capacities of the RGO/Si, S500, S650, and S800 samples were derived as 843, 777, 657, and 488 mAh g^{-1}, respectively.

Physicochemical properties of Si-based composites with different SiC contents

To assess the impact of SiC content on the physicochemical properties of Si-based composites, scanning electron microscopy (SEM), nitrogen adsorption/desorption test, tap density measurements, electrical conductivity measurements, Raman

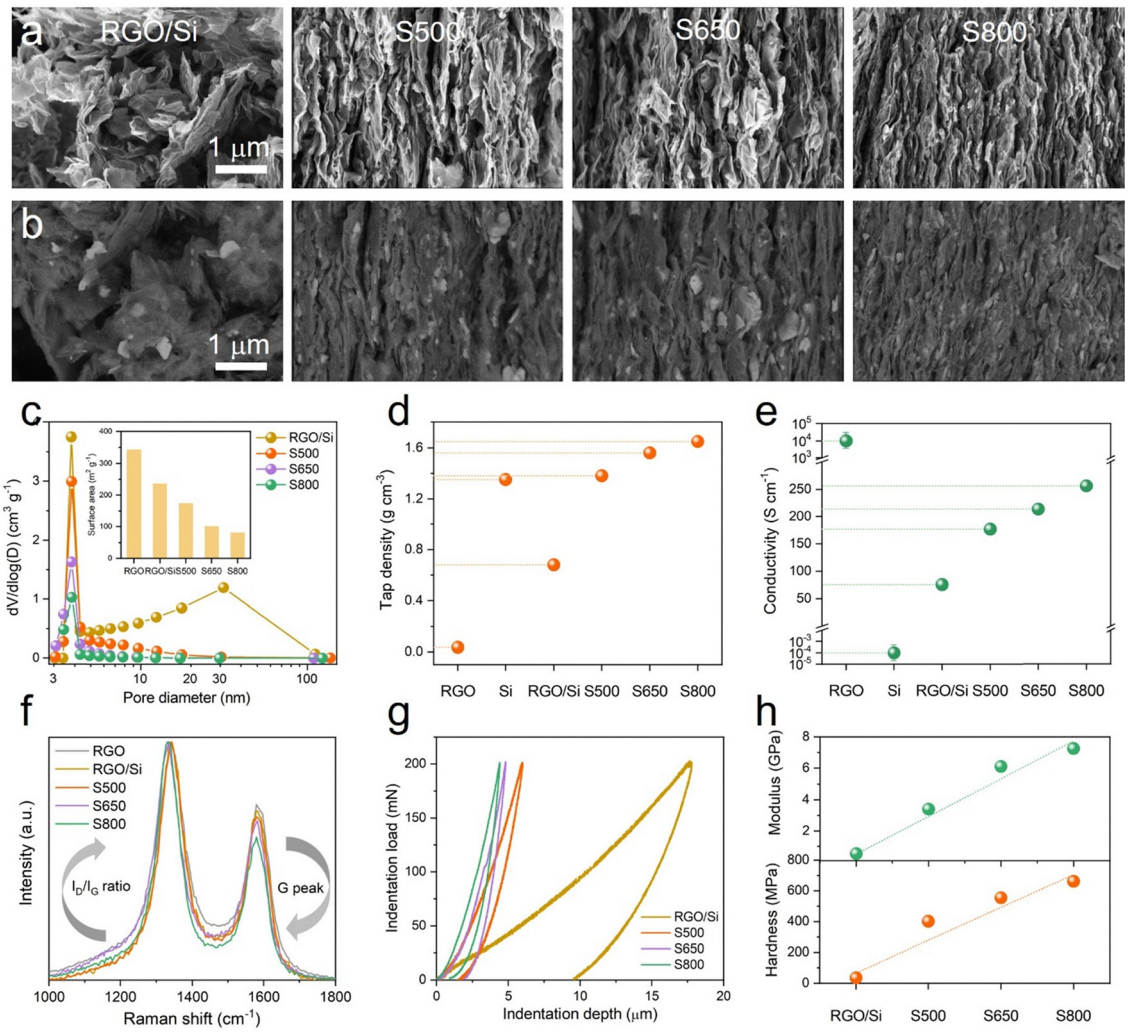

Fig. 3 Physicochemical properties of Si-based composites with different SiC contents. (a) and (b) SEM images of RGO/Si, S500, S650, and S800 samples in (a) secondary electron (SE) and (b) backscattered electron (BSE) mode. (c) Pore size distribution comparison of RGO/Si, S500, S650, and S800 samples, with their specific surface area in the inset. (d) Tap density comparison of Si-based composites. (e) Conductivity comparison of Si-based composites. (f) Raman spectra of RGO, RGO/Si, S500, S650, and S800. (g) Indentation test curves of RGO/Si, S500, S650, and S800. (h) Vickers hardness and Young's modulus comparison of RGO/Si, S500, S650, and S800.

spectroscopy, and indentation tests were carried out as shown in Fig. 3. The SEM images, as displayed in (ESI,† Fig. S2), reveal that RGO presented a petal-like lamellar structure with a lateral size of 5–10 μm and a thin thickness (consisting of 11–13 graphene layers), while the Si microparticles exhibited a rough surface with an average size of 1–3 μm. After the HEBM process, it is evident that RGO and Si particles were uniformly distributed within the RGO/Si composite in low-magnification SEM images, while parts of Si particles were fully wrapped in the thin graphene layer in high-magnification SEM images (Fig. 3(a), (b) and ESI,† Fig. S3). Besides, RGO/Si exhibited a porous structure with a certain number of pores and a reduced size of Si particles (100–300 nm). Similarly, the surface of the S500, S650, and S800 composites revealed homogeneous dispersion of Si particles, as shown in Fig. 3(a), (b) and ESI,† Fig. S4. Additionally, there were no obvious differences in the morphology of the SPS-processed Si-based composites. The overall morphology resembled well-scattered bark, with Si particles uniformly arranged among the bark-like structures, particularly evident in high-magnification SEM images, where some Si particles were seen to be enveloped or embedded between graphene layers. STEM and EELS mapping reveal that the surface of the Si particles was surrounded by a SiO_x layer, along with multiple graphene layers, which together provided protective shielding (ESI,† Fig. S5–S8).

Furthermore, by performing nitrogen adsorption/desorption isotherm tests on the Si-based composites, we analyzed their corresponding surface information using the Brunauer–Emmett–Teller (BET) and Barrett–Joyner–Halenda (BJH) methodologies (Fig. 3(c), Fig. S9, and Table S3, ESI†). From Fig. 3(c), it's noticeable that the total pore volume and average pore size progressively decreased from RGO/Si to S500, S650, and finally to S800. Their average pore size fell within the range of 5–8 nm, belonging to small mesoporous. Additionally, their specific surface areas exhibited a similar decreasing trend as the SPS temperature increased, measuring at 237 $m^2 g^{-1}$ for RGO/Si, 175 $m^2 g^{-1}$ for S500, 102 $m^2 g^{-1}$ for S650, and 81 $m^2 g^{-1}$ for S800.

Fig. 3(d) and (e) illustrate the tap density and electrical conductivity of the bare RGO, bare Si, RGO/Si, S500, S650, and S800 samples. The tap density of the RGO/Si composite was 0.68 g cm^{-3}, while the tap densities of Si-based composites after SPS treatment were measured as 1.38 g cm^{-3} (S500), 1.56 g cm^{-3} (S650), and 1.65 g cm^{-3} (S800), respectively (Fig. 3(d)). This indicates that the tap density of Si-based composites rises with the increase of SPS temperature, presumably due to the effect of SiC generation and SPS densification. Their electrical conductivity was recorded as 76 S cm^{-1} (RGO/Si), 177 S cm^{-1} (S500), 214 S cm^{-1} (S650), and 256 S cm^{-1} (S800), respectively (Fig. 3(e)). Despite incorporating high-conductivity RGO, the electrical conductivity of RGO/Si remained relatively low, possibly due to the porous structure of the composite, characterized by numerous voids. However, after SPS treatment, the overall density of the material increased, with a gradual reduction in pores and the formation of a denser structure, resulting in enhanced electrical conductivity (RGO accounts for a significant portion of the composite, thus it continues to make a substantial contribution to conductivity). Thus, even with the formation of SiC, the electronic conductivity of Si-based composites did not exhibit a notable decrease with the increase of SiC content. Furthermore, it should be noted that the high bulk electrical conductivity of the S800 sample does not imply enhanced Li^+ transport at the local interface. The thick and continuous SiC layer formed during high-temperature SPS possesses low ionic conductivity and electrochemical inertness, potentially hindering Li^+ diffusion into the Si core. This mismatch between electronic and ionic transport may lead to incomplete lithiation and suppressed capacity, despite the overall improvement in electronic conductivity.

Subsequently, we determined the degree of defect and disorder of Si-based composites by Raman spectra, as shown in Fig. 3(f) and ESI,† Fig. S10. The peak located at around 2900 cm^{-1} corresponded to the D + D′ peak, indicating the presence of RGO (ESI,† Fig. S10).[35] Moreover, the intensity ratio between the 2D peak and the G peak (I_{2D}/I_G) of 0.2 suggested the formation of multilayer graphene.[36] Fig. 3(f) illustrates a slight decrease in the intensity of the G peak from RGO to RGO/Si, S500, S650, and S800, indicating a gradual increase in the I_D/I_G ratio. Specifically, the I_D/I_G ratio increased from 1.35 for RGO to 1.39 for RGO/Si, 1.43 for S500, 1.49 for S650, and 1.67 for S800. This indicates that the degree of defects and disorder of the material was trending upward as the increase of SiC content.

The mechanical stability of Si-based composites with different SiC contents, such as Vickers hardness and Young's modulus, was derived by indentation testing (Fig. 3(g)). As shown in Fig. 3(h), the Vickers hardness values for RGO/Si, S500, S650, and S800 were recorded as 35.8, 402.4, 554.3, and 661.7 MPa, respectively, with the corresponding Young's modulus values of 0.5, 3.4, 6.1, and 7.3 GPa. These results suggest an enhancement in the mechanical strength of the material as the SPS temperature increases, attributed to the heightened SiC content and the effect of SPS densification.

Electrochemical properties of Si-based anodes with different SiC contents

The effects of different SiC contents on electrochemical properties of Si-based anode materials were evaluated, including specific capacity, initial coulombic efficiency (ICE), rate performance, and cycling stability, as shown in Fig. 4. By performing the first cycle of the charge–discharge voltage curve tests on the RGO/Si, S500, S650, S800 anodes (Fig. 4(a)), we obtained their corresponding specific capacity and ICE. As shown in Fig. 4(b), the specific capacities of RGO/Si, S500, S650, and S800 anodes at 0.1 A g^{-1} current density were 731, 674, 582, and 325 mAh g^{-1}, respectively. With the increase of SiC content, the capacity of Si-based anodes gradually decreased, which was consistent with the theoretical capacity change predicted by TGA. This phenomenon is attributed to the low-activity nature of SiC, which not only constrained the utilization of active Si's capacity but also resulted in a decrease in Si content, consequently reducing the overall electrode capacity. Besides, the ICE values of Si-based anodes were recorded as 41% (RGO/Si), 50% (S500), 52% (S650), and 53% (S800), respectively. The low ICE of RGO/Si was due to the incorporation of rGO, which possessed a high surface area and numerous defects, leading to increased side reactions during the formation of the solid electrolyte interphase (SEI). Interestingly, the ICE values of Si-based

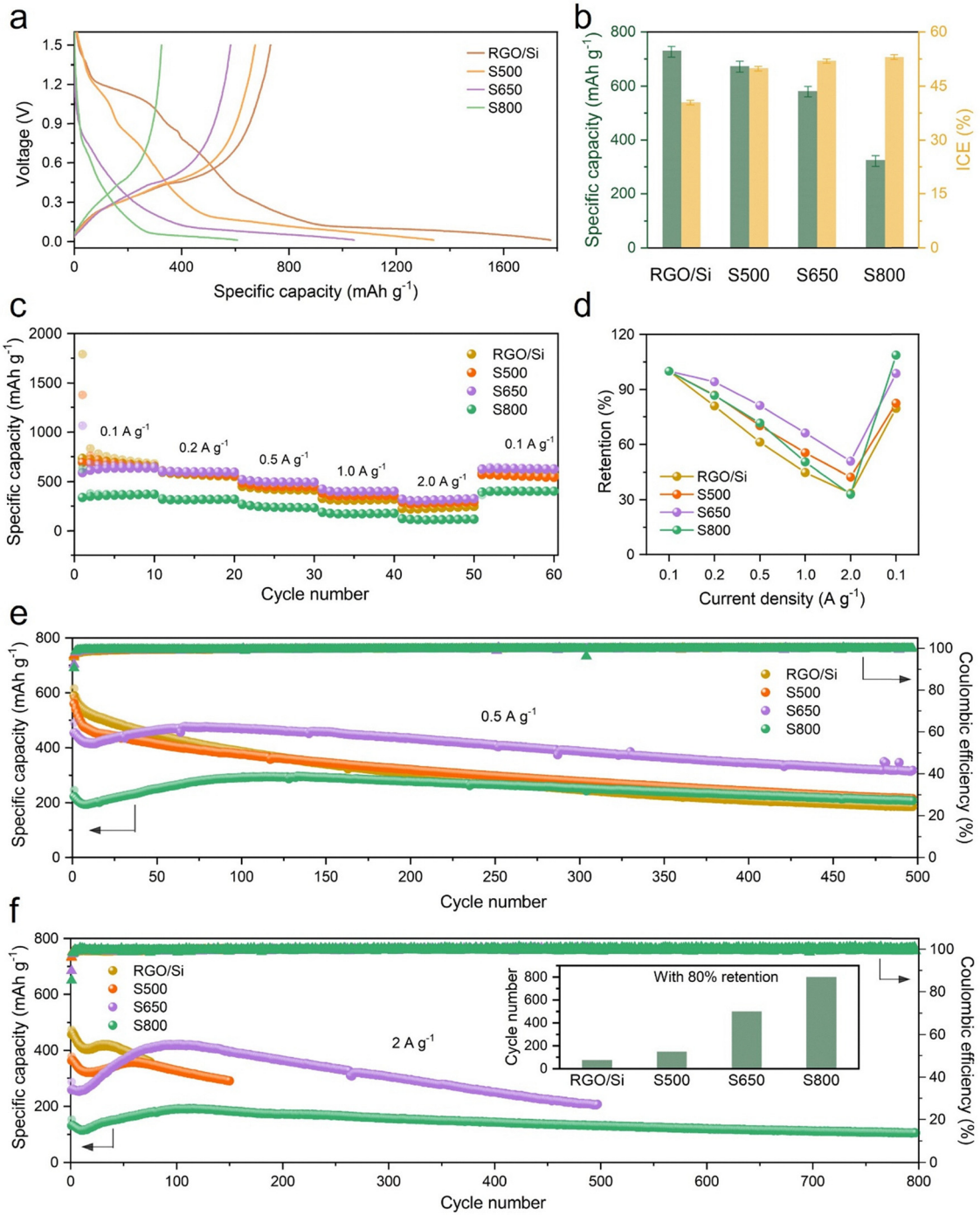

Fig. 4 Electrochemical properties of Si-based anodes with different SiC contents. (a) First cycle of the charge–discharge voltage curves of RGO/Si, S500, S650, and S800 anodes at 0.1 A g^{-1}. (b) Specific capacity and ICE comparison of RGO/Si, S500, S650, and S800 anodes. (c) Rate performance of RGO/Si, S500, S650, and S800 anodes at various current densities from 0.1 to 2 A g^{-1}. (d) The corresponding capacity retention comparison of Si-based anodes at various current densities. (e) Long cycling test of RGO/Si, S500, S650, and S800 anodes at 0.5 A g^{-1}. (f) Cycling stability comparison of RGO/Si, S500, S650, and S800 anodes at 2 A g^{-1}. The inset shows their corresponding cycle number when their capacity retention reaches 80%.

anodes with different SiC contents showed little variation, indicating that the SiC content had a minimal effect on ICE in this scenario. It is notable that the ICE increased after SPS treatment, likely due to the effects of SPS densification and purification, resulting in reduced surface area and functional groups. To address the relatively low ICE, several practical strategies can be considered: (1) reducing the ratio of binders and conductive additives (currently 20%, higher than typical industrial formulations, which may contribute to ICE loss); (2) optimizing electrolyte composition to suppress initial SEI formation; (3) employing prelithiation techniques; and (4) tailoring the RGO content and structure to minimize surface defects while preserving conductivity.

Similar results were also reflected in the cyclic voltammetry (CV) curves of Si-based anodes (ESI,† Fig. S11). The area of the CV curve gradually decreased from RGO/Si to S500, S650, and S800, indicating a gradually decreasing capacity. Besides, the peaks at 0.32 and 0.51 V corresponded to the delithiation reaction of Si, while the peaks at 0.21 V represented the lithiation process of Si. There were no peak of SiC observed in the reaction, since the reversible lithiation mechanism of SiC did not involve the formation of products like Li_xSi or Li_xC.[23] When compared to RGO/Si and S500, S650 and S800 anodes initially displayed lower peak currents in the early cycles. The peak intensity observed in the CV curve typically reflects the magnitude of the current, which is indicative of the insertion and extraction rates of Li ions in the Si anode, with larger peak intensities generally signifying faster Li-ion diffusion rates and enhanced electrode activity. As the SiC content increased from S500 to S650 and then to S800, the presence of SiC significantly restricted Li-ion transport due to its inherently inactive nature. This restriction resulted in a decreasing trend in the insertion and extraction rates of Li ions during the initial charge and discharge cycles.

Afterwards, the rate performance test of Si-based anodes was used to further analyze the Li ion/electron transport kinetics (Fig. 4(c) and (d)). After undergoing 10 cycles of the charge–discharge voltage tests at current densities ranging from 0.1 to 2 A g^{-1}, the current density was reverted to 0.1 A g^{-1}, and the corresponding capacity changes were recorded, as shown in Fig. 4(c). From RGO/Si to S500 and then S650, the rate performance improved progressively, with capacity retention at a current density of 2 A g^{-1} being 34% (245 mAh g^{-1}), 42% (292 mAh g^{-1}), and 51% (324 mAh g^{-1}), respectively (Fig. 4(d)). It is speculated that the dominant factor contributing to the improvement in rate performance was the increase in material conductivity facilitated by the enhanced SPS densification effect. However, when the SPS temperature was further raised to 800 °C, the rate capability of the S800 anode became worse, with a capacity retention of 33% (122 mAh g^{-1}) at 2 A g^{-1}. As the SiC content reached a certain threshold, the presence of thick SiC interface layers excessively covering the Si surface became the dominant factor, leading to a significant decrease in Li-ion transport efficiency.

Interestingly, despite the limitation or reduction in capacity caused by the presence of SiC in the Si-based anodes, their capacity gradually increased with the progression of the cycle numbers. For example, after multiple cycles, the specific capacity of the S650 anode escalated from an initial value of 582 mAh g^{-1} to a peak value of 637 mAh g^{-1} at 0.1 A g^{-1} (Fig. 4(c)). From a current density of 0.2 A g^{-1} onwards, its capacity gradually exceeded that of the RGO/Si and S500 anodes. Additionally, the capacity retention of the S800 anode surpassed 100% upon returning to 0.1 A g^{-1} current density, which was 109% (Fig. 4(d)). Certainly, the initial capacity of Si-based anodes was constrained by the presence of a SiC layer, limiting the transport efficiency of Li ions. However, with the increase in cycle numbers, the internal wettability of the anode improved gradually. The SiC layer may evolve into a Li-ion-rich phase, facilitating ion transport and reaction with Si, thereby progressively enhancing the capacity. This transformation may involve partial lithiation of SiC or occupation of Li^+ in interfacial defects, as suggested in previous studies,[22,23] indicating that SiC may serve as a limited Li^+ host after structural evolution.

To confirm our hypothesis, we further conducted electrochemical impedance spectroscopy (EIS) tests for Si-based anodes (ESI,† Fig. S12 and Table S4). After the first cycle of the charge–discharge voltage test, a stable SEI layer formed on the surface of the active materials. Compared to other samples (RGO/Si, S500, and S650), the S800 anode exhibited notably higher charge transfer resistance (R_{ct}) and ion diffusion resistance (Z_w). As predicted, the formation of a thick SiC interface significantly impedes the transport of electrons and ions to the electrode. However, after 500 cycles, the R_{ct} and Z_w values of the S800 anode decreased to the same level as other Si-based anodes, demonstrating that the transport dynamics of ions and electrons inside the SiC layer were improved after multiple cycles.

The cycling stability of Si-based anodes with different SiC contents was evaluated at current densities of 0.5 and 2 A g^{-1}, as shown in Fig. 4(e) and (f). After three activation cycles of 0.1 A g^{-1}, the charge and discharge cycling tests were carried out at 0.5 A g^{-1} for RGO/Si, S500, S650, and S800, with their initial capacities of 589, 560, 453, and 223 mAh g^{-1}, respectively (Fig. 4(e)). The specific capacities of RGO/Si and S500 anodes decreased rapidly with increasing cycle numbers, whereas the capacities of S650 and S800 anodes exhibited a gradual increase followed by a steady decline trend. Especially noteworthy is that after a certain number of cycles, the capacity of the S650 and S800 anodes surpassed that of the RGO/Si and S500 anodes. Consequently, after 500 cycles, their specific capacities were recorded as follows: 185 mAh g^{-1} for RGO/Si, 215 mAh g^{-1} for S500, 318 mAh g^{-1} for S650, and 207 mAh g^{-1} for S800, with the corresponding capacity retention of 31%, 38%, 70%, and 93%, respectively. Similarly, Si-based anodes with varying SiC contents exhibited a consistent curve change trend at a high rate of 2 A g^{-1} (Fig. 4(f)). In particular, when the capacity retention rate reached 80%, the corresponding cycle numbers for RGO/Si, S500, S650, and S800 anodes were 75, 150, 500, and 800, respectively. Therefore, it can be concluded that as the SiC content increases, the cycling stability of the Si-based anodes also improves, despite the decreasing initial capacity.

From the voltage profiles of various electrodes presented in ESI,† Fig. S13, it is evident that their discharge voltage platforms were predominantly centered around 0.2 V, aligning with the lithiation peak observed in the CV curve. Notably, the S800 electrode exhibited a steeper discharge voltage platform compared to the others, indicating that the insertion and extraction of Li ions was relatively unstable. This steepness suggests an uneven distribution of ions within the electrode material, leading to local variations in the reaction rate and resulting in rapid fluctuations in voltage. In terms of charge and discharge capacities, the 650 and S800 electrodes exhibited an initial decrease in capacity, followed by a subsequent increase. In contrast, the RGO/Si and S500 electrodes showed a more significant decline in capacity. These observations align with

the trends depicted in Fig. 4–6(c)–(f), suggesting that as the number of charge–discharge cycles increases, the internal wettability of the anode improves. This allows the SiC layer to transform into a Li-ion-rich phase, thereby enhancing ion transport and facilitating reactions with Si. As a result, this transformation contributes to a gradual increase in the anode's capacity over time.

To benchmark our Si–SiC–C composite against existing Si-based anodes, we provide a comparative summary in ESI,† Table S5. Notably, the S650 sample exhibits a balanced combination of high initial capacity (582 mAh g^{-1}), good rate performance (324 mAh g^{-1} at 2.0 A g^{-1}), long cycle life (500 cycles), and minimal electrode swelling (12.6%). These metrics compare favorably to previous works, highlighting the effectiveness of the engineered SiC interfacial layer in maintaining structural and electrochemical stability.

Swelling effect of Si-based anodes with different SiC contents

To explore the influence of different SiC contents on electrode swelling, we observed the cross-section and planar SEM morphology of the RGO/Si, S500, S650, and S800 anodes before and after 500 cycles (Fig. 5).

As shown in Fig. 5(a), the initial electrode thicknesses of the RGO/Si, S500, S650, and S800 anodes were measured at 39.6, 18.6, 16.7, and 12.2 μm, respectively. After 500 cycles, their thickness values increased to 65.9, 26.7, 18.8, and 13.3 μm for the RGO/Si, S500, S650, and S800 anodes, resulting in swelling rates of 66.4%, 43.5%, 12.6%, and 9.0%, respectively (Fig. 5(b)).

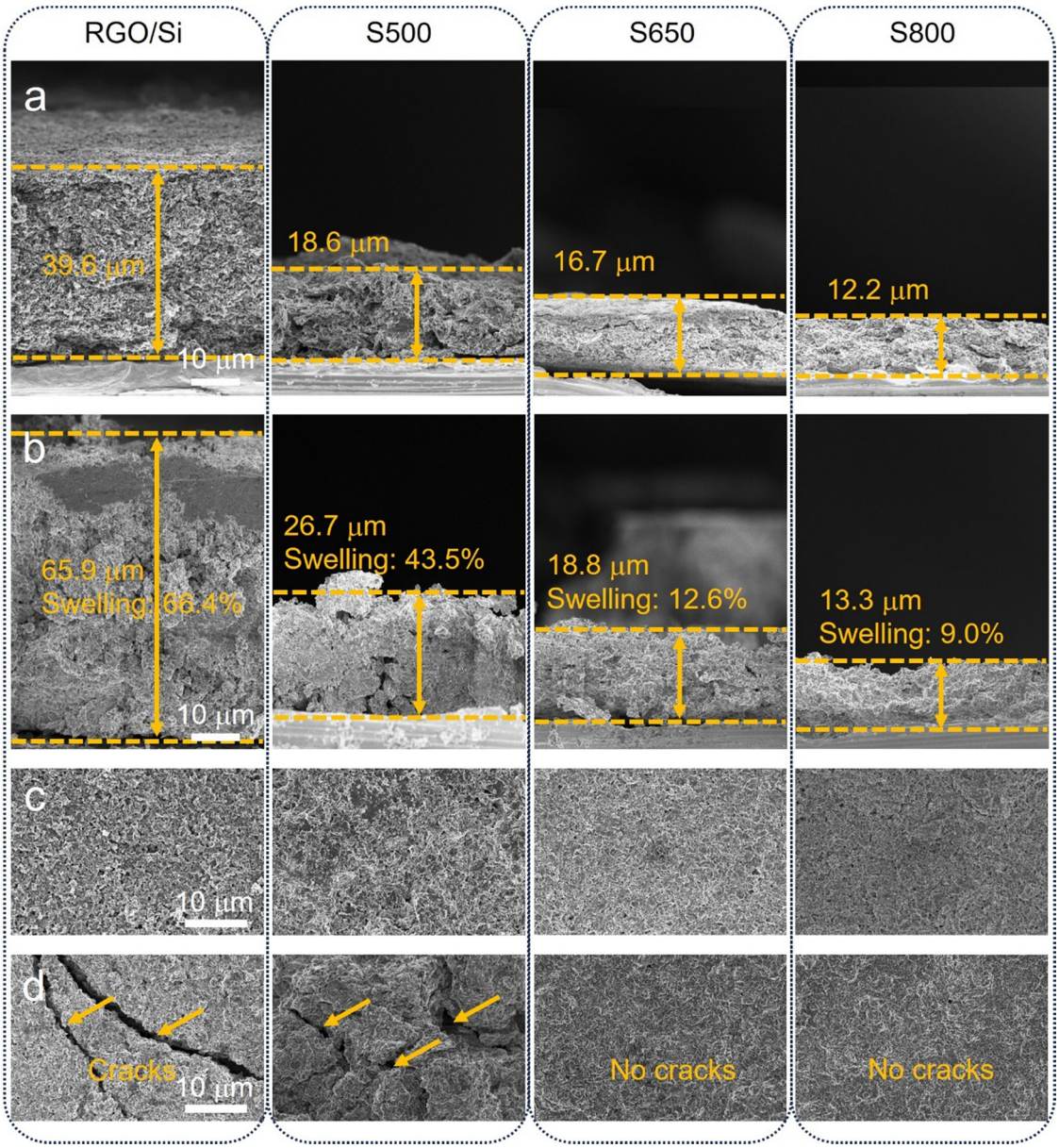

Fig. 5 Swelling effect of Si-based anodes with different SiC contents. (a) and (b) Cross-section SEM images of RGO/Si, S500, S650, and S800 electrodes (a) before and (b) after 500 cycles. (c) and (d) Planar SEM images of the RGO/Si, S500, S650, and S800 electrodes (c) before and (d) after 500 cycles.

Notably, the relatively small swelling observed in the S800 sample can be attributed to several factors. First, compared to the other samples, the S800 sample contains the lowest Si content (with Si, SiC, and RGO compositions of 8.9%, 16.4%, and 74.7%, respectively), which significantly reduces the overall expansion of the electrode. Second, RGO, which constitutes the majority of the material, exhibits a low expansion rate (<10%), further limiting electrode swelling. Additionally, the SiC layer, which covers most of the Si surface, has high mechanical strength and acts as a buffer layer. This buffer layer helps to maintain the structural integrity of the electrode even after repeated cycles of expansion and contraction. The higher the SiC content, the more obvious the protection effect.

Besides, it can be seen from the planar SEM images that the Si-based anodes exhibited a similar flat morphology before cycling (Fig. 5(c)). However, after 500 cycles, noticeable cracks and bumps were observed on the surfaces of the RGO/Si and S500 electrodes, whereas the surfaces of the S650 and S800 electrodes remained flat and continuous (Fig. 5(d)). It is noteworthy that the Si content in both the RGO/Si and S500 electrodes was relatively similar, at 21.1% and 18.8%, respectively. However, the S500 electrodes exhibited significant improvements in cycling stability and reduced swelling when compared to the RGO/Si electrodes. Therefore, it can be inferred that the introduction of a SiC layer is beneficial for Si-based anodes, as it helps to minimize electrode expansion. Furthermore, an increasing trend in electrode stability is observed with high SiC content, although the low Si content also appears to positively influence electrode stability.

Mechanism of SiC enhancing cycling stability in Si-based anodes

Fig. 6 shows the difference in the lithiation and delithiation processes of the Si-based anodes with different SiC contents. The thermodynamic and mechanical stability of the Si/SiC heterointerface plays a critical role in maintaining electrode integrity during cycling. Although first-principles calculations were not performed in this work, previous density functional

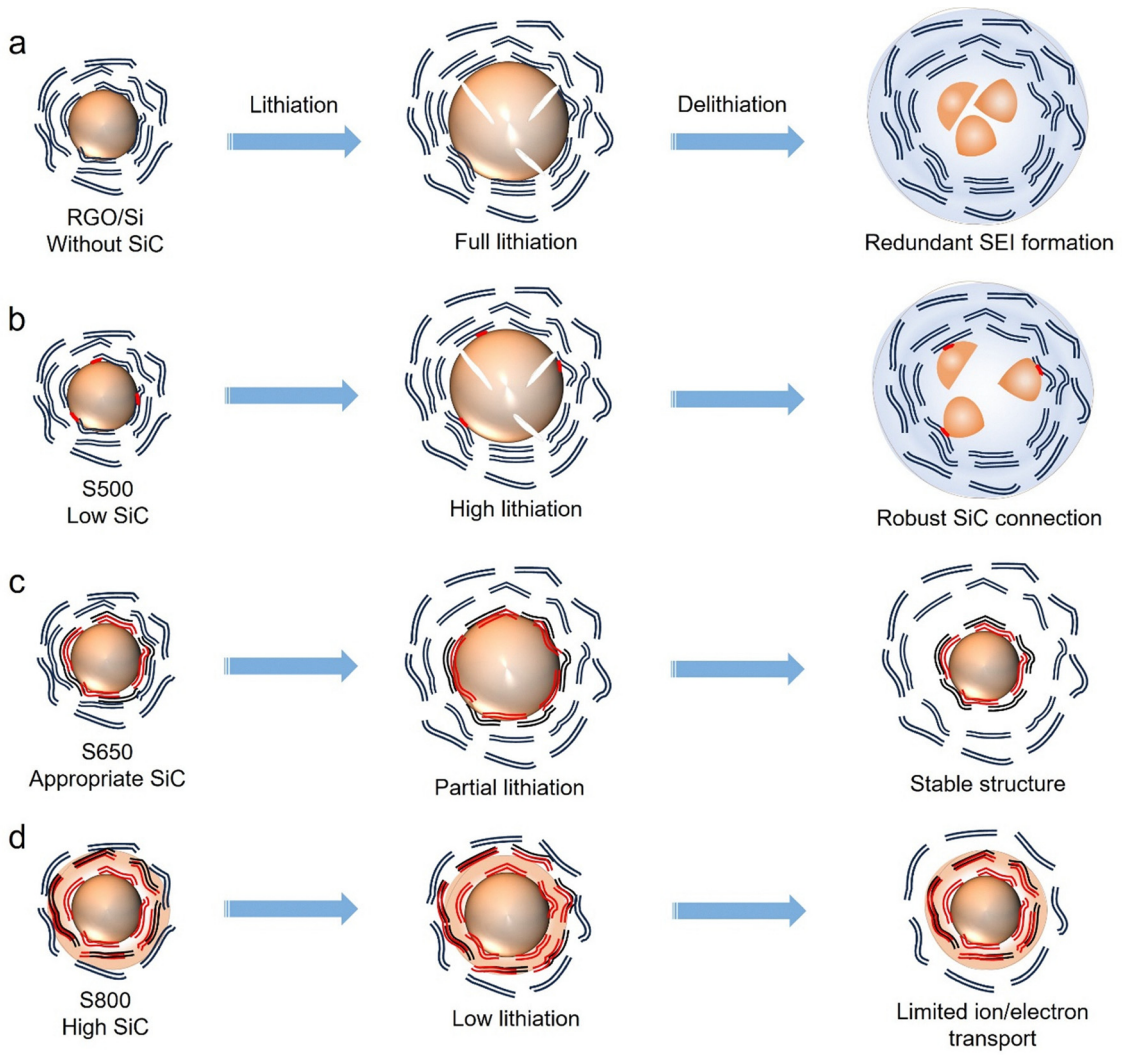

Fig. 6 Schematic diagram of the lithiation/delithiation process of Si-based anodes with different SiC content. (a)–(d) The lithiation/delithiation process of (a) RGO/Si, (b) S500, (c) S650, and (d) S800 anodes.

theory (DFT) studies have demonstrated strong interfacial binding between Si and SiC. For example, Sun *et al.* revealed that the Li^+ diffusion barrier at the Si/SiC interface is substantially reduced to 0.43 eV, compared to 0.84 eV in pristine SiC, as confirmed by DFT calculations.[22,23] Similarly, it has been reported that the SiC shell strongly stabilizes the Si core through robust covalent bonding.[20,21,37] These findings support our interpretation that the SiC layer reinforces the Si-based composite through a thermodynamically favorable interface, thereby improving structural durability during repeated lithiation and delithiation.

For the RGO/Si anode, as there is no SiC interfacial layer in the composite, the highest capacity can be achieved through complete lithiation, leading to full expansion (Fig. 6(a)). Consequently, the Si particles are prone to fracture due to the significant strain exerted on them. During the delithiation process, redundant SEI is repeatedly formed near the broken Si particles, resulting in the worst cycling stability. For the S500 anode, despite the presence of a small amount of SiC interfacial layer, a significant degree of lithiation reaction can still occur, allowing for considerable expansion and achieving high capacity (Fig. 6(b)). However, this high expansion also leads to the fragmentation of Si particles. Upon delithiation, repeated SEI is generated near the fractured Si particles, contributing to poor cycling stability. Unlike the RGO/Si anode, the SiC interface layer in the S500 anode consistently maintains the connection between Si and carbon, ensuring effective electrical contact throughout cycling, even in the event of Si particle breakage.

In contrast, the S650 anode possesses an optimal SiC interfacial layer content, enabling partial lithiation reaction within the Si particles to achieve a moderate specific capacity (Fig. 6(c)). The robust SiC interfacial layer discretely covers the surface of the Si particles, limiting expansion while reducing strain and ultimately preventing the Si particles from breaking. Throughout the delithiation process, the structural integrity remains intact, courtesy of the high mechanical strength of SiC. Additionally, the chemical stability of SiC prevents further interaction between the Si core and the electrolyte, thereby preventing the generation of excessive SEI. Moreover, the SiC layer consistently upholds an effective connection between Si and carbon, establishing a stable channel for ion and electron transport and a steady electrode structure, thereby ensuring enduring cycling stability.

As for the S800 anode, characterized by a high SiC interfacial layer content, Li ions encounter difficulty in penetrating and reacting with the Si core, resulting in minimal expansion and serious capacity reduction (Fig. 6(d)). Consequently, the robust and thick SiC layer shields the Si particles from significant strain, preventing their breakage. During delithiation, the electrode maintains a stable Si–SiC–C heterostructure without generating excessive SEI. Since SiC ensures the connection of continuous Si–C interfaces and maintains the integrity of the electrode, the S800 anode exhibits excellent cycling stability. Nonetheless, the transport efficiency of electrons and ions is significantly impaired as the thick SiC layer, with its inactive and low-conductivity nature, covers most of the Si core surface. Fortunately, with the continuous processes of lithiation and delithiation, the internal wettability of the active material is gradually improved. With the continuous penetration of Li ions into the SiC layer, it evolves into a Li-ion-rich phase, which is conducive to ion transport and reaction with Si cores, resulting in a gradual increase in capacity. This is supported by EIS results, which show a notable decrease in charge transfer and diffusion resistance after cycling, indicating enhanced ionic accessibility. Similar behavior has been reported in previous studies, where repeated lithiation leads to partial lithiation or structural transformation of SiC-related interphases into more Li^+-permeable configurations.[22,23]

Hence, an optimal SiC content ($\sim$10%), characterized by its high mechanical and chemical stability, upholds the structural integrity of Si-based anodes during the lithiation/delithiation process, thereby preserving cycling stability. This moderate SiC content strikes a balance, avoiding excessive consumption of the active Si core, thus ensuring a reasonable electrode capacity. More importantly, as the lithiation advances, the SiC layer undergoes a transformation into a Li-ion-rich phase, facilitating ion transport and subsequent reactions with the Si core, thus further augmenting the electrode's capacity. The SiC interfacial layer (in S650), being discreetly distributed, does not hinder the contact between Li ions and the Si core entirely, ensuring efficient ion and electron transport dynamics, thereby sustaining the electrode's rate performance. While the composite consists of RGO, Si, and SiC, the specific electrochemical roles of each component are closely interlinked and difficult to decouple quantitatively. RGO contributes to electronic conductivity and mechanical flexibility, Si serves as the main lithium storage phase, and the SiC layer offers structural protection and evolving ionic pathways during cycling. Notably, the ionic conductivity and capacity contribution of SiC are not static but increase progressively with cycling due to structural evolution, as supported by EIS and capacity recovery data. This dynamic behavior makes it experimentally challenging to isolate the contribution of each phase through individual cycling tests. Nevertheless, the observed trends in initial capacity, rate performance, and long-term stability can be well understood in terms of their combined and synergistic functions.

Discussion

In conclusion, we successfully controlled the thickness/content of the SiC interfacial layer in the Si–SiC–C heterostructure using modified SPS technology. With the increase of SPS temperature, the SiC interfacial layer content increased, resulting in Si-based composites with reduced pore structure and a lower specific surface area. Additionally, the tap density and electrical conductivity of the Si-based composites increased, accompanied by enhancements in degrees of defect and disorder, as well as mechanical strength parameters such as Vickers hardness and Young's modulus. The alteration in the physical and chemical properties of the Si-based anode also directly impacts its electrochemical performance, *e.g.*, the increase in SiC content improved

the cyclic stability of the Si-based composites at the expense of specific capacity. Hence, the S650 anode, with 10.2% SiC content, exhibited the most reliable electrochemical performance compared to the RGO/Si (0%), S500 (3.0%), and S800 (16.4%) anodes. Specifically, the S650 anode delivered an initial capacity of 582 mAh g^{-1} (0.1 A g^{-1}), excellent cycle stability (500 cycles with 80% capacity retention), good rate capability (324 at 2 A g^{-1}), and a low electrode swelling rate of 12.6%. Furthermore, after multiple cycles, the specific capacity of the S650 anode could be increased to a maximum of 637 mAh g^{-1} at 0.1 A g^{-1}. This phenomenon is due to the SiC layer gradually transitioning into a Li-ion-rich phase, facilitating ion transport and reaction with Si, thereby leading to a gradual increase in capacity. Consequently, it is evident that the SiC interfacial layer plays a crucial role in enhancing the mechanical stability of the Si-based anodes. The incorporation of the SiC interfacial layer is anticipated to bolster the structural integrity between Si and carbon, while minimizing its effects on capacity and ion/electron transport kinetics. This is anticipated to yield reliable Si-based anodes with a high Si content.

Methods

Preparation of RGO/Si composite

The RGO/Si composite was fabricated by the high-energy ball milling (HEBM) method. Specifically, 1 g of reduced graphene oxide (RGO, 99%, purchased from Dazhan Nanomaterials Co., LTD) powder and 0.25 g of silicon micropower (Si, 99.9%, purchased from US Research Nanomaterials, Inc.) were mixed in alcohol solution. After ultrasonic dispersion for 1 h, HEBM was performed at a speed of 500 rpm for 8 h. A homogeneously distributed RGO/Si composite powder was then obtained following a 12 h vacuum drying process at 100 °C.

Preparation of S500, S650, and S800 composites

The S500, S650, and S800 composites were fabricated by the modified spark plasma sintering (SPS, KCE®-FCT H-HP D 25-SD, FCT Systeme GmbH) process.[26] The modified SPS system, as shown in Fig. 1(a), employs tungsten carbide (WC) as the mold and the insulating foil acting as the lining, allowing pulsed current and pressure to be applied directly to the powder. Specifically, 2 g RGO/Si powder was placed in the WC mold, followed by insertion into the vacuum chamber. The SPS pressure was controlled at 120 MPa, with a ramping temperature of 25 °C min^{-1} and a holding time of 30 min, while the sintering temperature was precisely controlled at 500, 650, and 800 °C, respectively, to obtain S500, S650, and S800 blocks. Through the ball milling method, the blocks were further crushed, resulting in the production of S500, S650, and S800 composite powders.

Material characterization

The morphologies and cross-sectional investigation were carried out using field emission scanning electron microscopy (SEM, VERIOS 460, FEI) and scanning transmission electron microscope (S/TEM, Titan Themis^3 S/TEM, FEI). The structural information and chemical composition were investigated by using X-ray photoelectron spectroscopy (XPS, Escalab 250Xi, Thermo Fisher Scientific), thermal gravimetric analysis (TGA, Q500, TA Instruments), Raman microscope (Alpha 300R, WITec), and X-ray diffractometer (XRD, D8 Advance, Bruker). The nitrogen adsorption–desorption analyzer (Quadrasorb EVO, Quantachrome) and nanoindenter test (Hysitron TI 980 Triboindenter, Bruker) were conducted to investigate the physical properties.

Electrochemical characterization

The working electrodes were created by grinding 80% active materials (RGO/Si, S500, S650, and S800), 10% Super P, and 10% binder (sodium carboxymethyl cellulose and styrene-butadiene rubber with a mass ratio of 1 : 1) into a uniform slurry. The slurry was then coated onto a copper current collector and dried at 100 °C for 12 h, with a mass loading control of 1.0–1.5 mg cm^{-2} for active materials. The electrochemical tests were conducted using CR2032 coin cells, with Si-based anodes (RGO/Si, S500, S650, and S800) acting as the working electrode, Li foil as the counter and reference electrode, 1.0 M $LiPF_6$ in ethylene carbonate/diethyl carbonate (EC/DEC, 1 : 1 vol%) with 10 wt% fluoroethylene carbonate (FEC) as the electrolyte, and polypropylene (Celgard 2400) as the separator. The battery performance was evaluated by galvanostatic charge/discharge, cyclic voltammetry (CV), and electrochemical impedance spectroscopy (EIS) measurements conducted on a LAND testing system and a VSP-300 electrochemical station at room temperature in the potential window between 0.01 and 1.5 V. Specifically, after completing the activation process (at 0.1 A g^{-1} for the first 3 cycles), the long-term galvanostatic charge/discharge tests were conducted at current densities of 0.5 and 2 A g^{-1}, respectively. Besides, EIS testing was conducted in the frequency range of 100 kHz to 0.01 Hz, whereas CV measurements were conducted at a scan rate of 0.1 mV s^{-1}. The specific capacities of Si-based anodes were calculated based on the total amount of active mass loading.

Author contributions

B. Ö. supervised the project. W. L. and J. H. L. designed and carried out the experiments. Y. Y., and M. L. performed TEM, STEM, and EELS characterization. W. L., J. H. L., and B. Ö. discussed and analyzed the experimental results and the writing of the paper. Y. K. O., C. L., L. S., Y. P., and Y. R. participated in the discussion of the project, contributed to materials characterization and provided experimental assistance.

Data availability

The data supporting this article have been included as part of the ESI.†

Conflicts of interest

The authors declare no competing interests.

Acknowledgements

This work was supported by the National Research Foundation, Prime Minister's Office, Singapore, under its Competitive Research Programme (CRP award number NRFCRP22-2019-8), and Medium-Sized Centre Programme (CA2DM), by the Ministry of Education of Singapore, under its Research Centre of Excellence award to the Institute for Functional Intelligent Materials (I-FIM, project no. EDUNC-33-18-279-V12), and EDB Singapore, under its Space Technology Development Programme (S22-19013-STDP), and Agency for Science, Technology and Research (A*STAR), under its LCER Phase 2 Programme, HET FI (grant no. U2411D4008). M. L. acknowledges support from the Opportunity Fund Project 2023 under PID URF/1/5578-01-01 of the King Abdullah University of Science and Technology.

References

1 W. Yan, *et al.*, Hard-carbon-stabilized Li–Si anodes for high-performance all-solid-state Li-ion batteries, *Nat. Energy*, 2023, **8**, 800–813, DOI: **10.1038/s41560-023-01279-8**.
2 Z. Lin, *et al.*, Aligning academia and industry for unified battery performance metrics, *Nat. Commun.*, 2018, **9**, 5262, DOI: **10.1038/s41467-018-07599-8**.
3 J. T. Frith, *et al.*, A non-academic perspective on the future of lithium-based batteries, *Nat. Commun.*, 2023, **14**, 420, DOI: **10.1038/s41467-023-35933-2**.
4 M. Ge, *et al.*, Recent Advances in Silicon-Based Electrodes: From Fundamental Research toward Practical Applications, *Adv. Mater.*, 2021, **33**, e2004577, DOI: **10.1002/adma.202004577**.
5 X. Zhang, *et al.*, Stable high-capacity and high-rate silicon-based lithium battery anodes upon two-dimensional covalent encapsulation, *Nat. Commun.*, 2020, **11**, 3826, DOI: **10.1038/s41467-020-17686-4**.
6 Z. Zhao, *et al.*, Revival of Microparticular Silicon for Superior Lithium Storage, *Adv. Energy Mater.*, 2023, **13**, 2300367, DOI: **10.1002/aenm.202300367**.
7 X. Xiong, *et al.*, $Li_4Ti_5O_{12}$ coating on copper foil as ion redistributor layer for stable lithium metal anode, *Adv. Energy Mater.*, 2022, **12**, 2103112, DOI: **10.1002/aenm.202103112C**.
8 J.-M. Yoon, *et al.*, Recent advances in Sb-based anodes for Li/Na/K-ion batteries and all-solid-state Li-ion batteries, *Energy Mater.*, 2024, **4**, 400063, DOI: **10.20517/energymater.2023.146**.
9 L. Huang, *et al.*, Engineering of lithiophilic hosts for stable lithium metal anodes, *Energy Mater.*, 2024, **4**, 400030, DOI: **10.20517/energymater.2023.83**.
10 Z. Li, *et al.*, Covalent Coating of Micro-Sized Silicon With Dynamically Bonded Graphene Layers Toward Stably Cycled Lithium Storage, *Adv. Energy Mater.*, 2023, **13**, 2300874, DOI: **10.1002/aenm.202300874**.
11 T. Lee, *et al.*, Suppressing Deformation of Silicon Anodes via Interfacial Synthesis for Fast-Charging Lithium-Ion Batteries, *Adv. Energy Mater.*, 2023, **13**, 2301139, DOI: **10.1002/aenm.202301139**.
12 Y. Zhang, *et al.*, Anchoring silicon on the basal plane of graphite via a three-phase heterostructure for highly reversible lithium storage, *Energy Storage Mater.*, 2021, **34**, 311–319, DOI: **10.1016/j.ensm.2020.10.002**.
13 J. Sung, *et al.*, Subnano-sized silicon anode via crystal growth inhibition mechanism and its application in a prototype battery pack, *Nat. Energy*, 2021, **6**, 1164–1175, DOI: **10.1038/s41560-021-00945-z**.
14 M. Furquan, *et al.*, Mechanical and Electrochemical Stability Improvement of SiC-Reinforced Silicon-Based Composite Anode for Li-Ion Batteries, *ACS Appl. Energy Mater.*, 2020, **3**, 12613–12626, DOI: **10.1021/acsaem.0c02523**.
15 Y. Jiang, *et al.*, Interfacial engineering of Si/multi-walled carbon nanotube nanocomposites towards enhanced lithium storage performance, *Carbon*, 2016, **107**, 600–606, DOI: **10.1016/j.carbon.2016.06.068**.
16 Z. Chen, *et al.*, In Situ Generation of Few-Layer Graphene Coatings on SnO_2–SiC Core–Shell Nanoparticles for High-Performance Lithium-Ion Storage, *Adv. Energy Mater.*, 2012, **2**, 95–102, DOI: **10.1002/aenm.201100464**.
17 M. Gautam, *et al.*, Design of Low-Stress robust silicon and Silicon-Carbide anode with high areal capacity and high energy density for Next-Generation Lithium-Ion batteries, *Chem. Eng. J.*, 2023, **472**, 144916, DOI: **10.1016/j.cej.2023.144916**.
18 W. Zhou, *et al.*, Introducing SiC/C dual-interface on porous silicon anode by a conventional exothermic displacement reaction for improved cycle performance, *J. Power Sources*, 2021, **508**, 230326, DOI: **10.1016/j.jpowsour.2021.230326**.
19 C. Yu, *et al.*, Silicon Carbide as a Protective Layer to Stabilize Si-Based Anodes by Inhibiting Chemical Reactions, *Nano Lett.*, 2019, **19**, 5124–5132, DOI: **10.1021/acs.nanolett.9b01492**.
20 H. Li, *et al.*, Bowl-like 3C-SiC Nanoshells Encapsulated in Hollow Graphitic Carbon Spheres for High-Rate Lithium-Ion Batteries, *Chem. Mater.*, 2016, **28**, 1179–1186, DOI: **10.1021/acs.chemmater.5b04750**.
21 R. Nandan, *et al.*, Zinc blende inspired rational design of a β-SiC based resilient anode material for lithium-ion batteries, *J. Mater. Chem. A*, 2022, **10**, 5230–5243, DOI: **10.1039/d1ta08516f**.
22 C. Sun, *et al.*, High-Quality Epitaxial N Doped Graphene on SiC with Tunable Interfacial Interactions via Electron/Ion Bridges for Stable Lithium-Ion Storage, *Nano-Micro Lett.*, 2023, **15**, 202, DOI: **10.1007/s40820-023-01175-6**.
23 C. Sun, *et al.*, Interfacial coupled design of epitaxial Graphene@SiC Schottky junction with built-in electric field for high-performance anodes of lithium ion batteries, *Nano Energy*, 2020, **77**, 105092, DOI: **10.1016/j.nanoen.2020.105092**.
24 R. Raccichini, *et al.*, The role of graphene for electrochemical energy storage, *Nat. Mater.*, 2015, **14**, 271–279, DOI: **10.1038/nmat4170**.
25 S. T. Pantelides, Defects in amorphous silicon: A new perspective, *Phys. Rev. Lett.*, 1986, **57**, 2979, DOI: **10.1103/PhysRevLett.57.29792979**.
26 W. Lai, *et al.*, High mechanical strength Si anode synthesis with interlayer bonded expanded graphite structure for lithium-ion batteries, *J. Energy Chem.*, 2024, **93**, 253–263, DOI: **10.1016/j.jechem.2024.02.021**.
27 S. Park, *et al.*, Scalable Synthesis of Hollow beta-SiC/Si Anodes *via* Selective Thermal Oxidation for Lithium-Ion

Batteries, *ACS Nano*, 2020, **14**, 11548–11557, DOI: 10.1021/acsnano.0c04013.

28 J. Trapp and B. Kieback, Fundamental principles of spark plasma sintering of metals: part I – Joule heating controlled by the evolution of powder resistivity and local current densities, *Powder Metall.*, 2019, **62**, 297–306, DOI: 10.1080/00325899.2019.1653532.

29 W. Zhou, *et al.*, Interface Engineering of Silicon and Carbon by Forming a Graded Protective Sheath for High-Capacity and Long-Durable Lithium-Ion Batteries, *ACS Appl. Mater. Interfaces*, 2021, **13**, 15216–15225, DOI: 10.1021/acsami.1c00107.

30 J. Su, *et al.*, Large-Scale Synthesis and Mechanism of β-SiC Nanoparticles from Rice Husks by Low-Temperature Magnesiothermic Reduction, *ACS Sustainable Chem. Eng.*, 2016, **4**, 6600–6607, DOI: 10.1021/acssuschemeng.6b01483.

31 P. Cavaliere, *Spark plasma sintering of materials: advances in processing and applications*, Springer, 2019.

32 Z. A. Liu, *et al.*, Solution-catalyzed carbothermal reduction of argo-waste SiO_2 enables low-temperature and fast synthesis of Si(II)–C anode, *Chem. Eng. J.*, 2023, **472**, 145116, DOI: 10.1016/j.cej.2023.145116.

33 Y.-R. Luo and J. A. Kerr, *CRC handbook of chemistry and physics*, CRC Press, Boca Raton, New York, 2012, vol. 89, pp. 65–98.

34 B. E. Nilssen, *et al.*, The distribution of oxygen in submicron silicon powders produced by ultrafine grinding, *Powder Technol.*, 2023, **427**, 118657, DOI: 10.1016/j.powtec.2023.118657.

35 D. R. Shaw, *et al.*, Extracellular electron transfer-dependent anaerobic oxidation of ammonium by anammox bacteria, *Nat. Commun.*, 2020, **11**, 2058, DOI: 10.1038/s41467-020-16016-y.

36 X. Li, *et al.*, Large-area synthesis of high-quality and uniform graphene films on copper foils, *Science*, 2009, **324**, 1312–1314, DOI: 10.1126/science.117124.

37 A. Majid, *et al.*, Assessment of 2H–SiC based intercalation compound for use as anode in lithium ion batteries, *Ceram. Int.*, 2020, **46**, 5297–5305, DOI: 10.1016/j.ceramint.2019.10.280.

